# Numerical Simulations of Isotropic and Orthotropic Flexible Hydrofoils in Calm Water and Head Waves

K.I. Matveev, M.P. Wheeler (Washington State University, USA)

#### **ABSTRACT**

Hydrofoils and their derivates are often used for generating lift forces to support boat weight, control its motions and provide thrust. With advances in manufacturing of composites, these materials present a promising alternative to replace metals in hydrofoil applications due to higher specific strength and damping, as well as potential for self-adaptability. However, higher flexibility and more complicated failure processes in hydrofoils made of composites require better understanding and accurate modeling of flexible hydrofoil behavior in sea conditions, especially in unsteady situations.

This paper focuses on high-fidelity simulations surface-piercing hydrofoils using coupled computational fluid dynamics and finite element analysis. Several hydrofoil materials are considered, including perfectly rigid, isotropic and orthotropic structures. Orthotropic materials can serve as models for fiber-reinforced polymers. In this study, the effect of the fiber orientation on the hydrofoil hydroelastic response has been numerically investigated in both calm water and regular head waves. Variations of the lift coefficient, twist, tip displacements and stresses are reported in the range of explored conditions. The orthotropic hydrofoil with the spanwise fiber orientation is found to behave similarly to isotropic and rigid hydrofoils. With the fibers originating at the hydrofoil root and directed toward the hydrofoil leading edge, negative twist and lower lift coefficients are found in calm-water conditions, while the fiber orientation toward the trailing edge leads to higher twist and rise in the lift force. The hydrofoil bending increases with deviation of the fibers from the spanwise direction. In the presence of head waves, hydrofoils with the fiber orientation toward the leading edge exhibit lower oscillations of the lift coefficient, whereas the fiber direction toward the trailing edge leads to larger structural oscillations. These findings present opportunities for designing hydrofoils with load-dependent hydrodynamic characteristics.

## INTRODUCTION

Hydrofoils are the streamlined solid bodies intended for generating large lift forces in a direction perpendicular to the incident water flow, while keeping drag forces parallel to the flow relatively low. Hydrofoils can be used to carry entire or partial weight of fast marine vehicles by elevating hulls and thus reducing or completely eliminating the hull water drag. Hydrofoils are commonly applied as control surfaces (rudders, fins) on boats and ships and as devices extracting energy from flowing water in some ocean-based renewable energy systems. Cross-sections of propellers and waterjet impellers also utilize hydrofoil shapes to efficiently generate thrust.

In the past, hydrofoils were broadly used on fast ferries, as well as recreational and intercepting boats (Acosta, 1973). In the optimal operational regimes, e.g., at speeds 30-40 knots for hulls of 50 to 100-ton displacements, many passenger-carrying hydrofoil ships had the lift-to-drag ratios (LDR) of 13-14, which are substantially higher than LDR of simpler planing boats. However, in off-design loadings and speed conditions, hydrofoils usually produce excessive drag or inadequate lift, which limits a range of their applications. For example, hydrofoil lift, which is roughly proportional to the speed squared, becomes inadequate at low speeds to elevate a boat hull. At sufficiently high speeds, vaporous cavitation and air ventilation on the suction sides of hydrofoils may result in lift reduction as well. Controlling orientations of hydrofoil system elements can partly alleviate these problems, but leads to increased complexity and cost. Hydrofoil systems applied on most ships and boats built in the last century were made of primarily metal alloys. Their large weights and difficulty in servicing such systems also decrease the hydrofoil appeal despite hydrodynamic advantage.

With the present availability of significantly lighter composite materials, hydrofoils recently started reappearing on fast sailing yachts and surfboards (Keller, et al., 2016; Giovannetti, et al., 2018). Weight reduction, easier servicing, higher damping, higher strength-to-weight ratio, and a potential for self-adaptability (e.g.,

decreasing lift coefficient at higher speeds) make composite hydrofoils very attractive for marine applications. With further advances in the composite technology and manufacturing, hydrofoils and other lift-generating devices (propellers, rudders, etc.) made of fiber-reinforced materials are likely to find more applications on future ships and powerboats. Flexible hydrofoils can also be used for augmenting air cavities formed under hulls of ships with air-injection drag reduction systems (Collins & Matveev, 2019).

Despite the apparent advantage of composite materials being lighter, there are challenges associated with more complicated internal structure and usually higher flexibility of such materials. One example of deformed hydrofoils numerically simulated in this study in calm water is shown in Figure 1. Complicated fluidstructure interactions of composite hydrofoils make it more difficult to predict their hydrodynamic performance, especially in unsteady environments, and to assess their structural dynamics. Even more challenging are the situations with the air-water interfaces, when waves and air ventilation phenomena become important (Young, et al., 2017; Matveey, et al., 2019). Therefore, there is a strong need for high-fidelity computational approaches that can model coupled problems dynamic involving free-surface hydrodynamics and anisotropic lift-generating flexible solid structures.

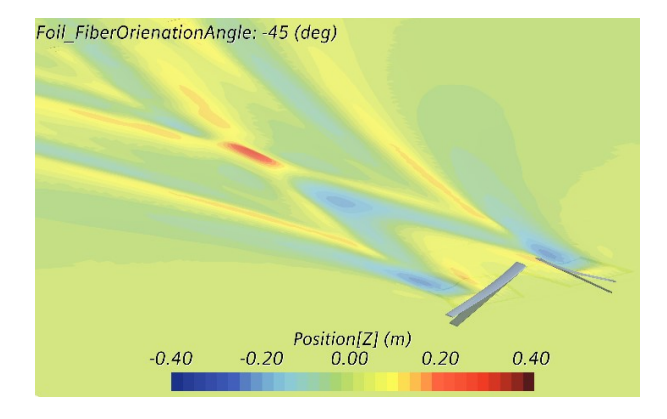


**Figure 1:** Example of simulated wave pattern behind translating flexible hydrofoils. Lower foil image shows original (non-deformed) hydrofoils.

A number of experimental and computational studies of flexible lifting devices in water flows have been carried out, especially in recent years. Ducoin, *et al.* (2009) experimentally and numerically investigated a deformable hydrofoil that spanned almost entire width of a water tunnel. Some of their test results are used in this paper for the verification and validation of the present

numerical approach. Blasques, et al. (2010) developed a computational model involving a boundary element method (BEM) and finite-element method (FEM) for analysis and optimization of a composite marine propeller and showed that it could outperform its metal counterpart. Zarruk, et al. (2014) conducted an extensive experimental study with several hydrofoils of different materials, including composites. Hydrofoils were tested in a water tunnel, and both hydrodynamic and vibration characteristics were recorded. Akcabay & Young (2015) developed a simplified reduced-order model for flexible foils that can provide a quick estimation for primary response frequencies of hydrofoils in unsteady cavitating flows. Harwood (2016) investigated both rigid and flexible hydrofoils by carrying out towing tank tests and theoretical modeling, paying special attention to regimes when one side of hydrofoils was ventilated with atmospheric air. Wu, et al. (2018) explored flow structure of cloud cavitation around a flexible foil focusing on vibration and cavity shedding. Liao, et al. (2019) analyzed hydroelastic response of composite hydrofoils in the uniform incident water flow using computational fluid dynamics (CFD) and FEM. They investigated the influence of fiber orientations on the vibration characteristics and bend-twist coupled behavior in single-phase flow. Young, et al. (2019) studied hydroelastic response of composite hydrofoils experimentally and by using simplified models. They found that hydrofoils with nose-up twist exhibit higher lift coefficients and earlier stall. Unsteady simulations of surface-piercing flexible hydrofoils made of uniform (isotropic) materials have been initiated by Wheeler & Matveev (2019).

The focus of the present work is on high-fidelity CFD-FEM modeling of surface-piercing dihedral hydrofoils with different structural properties (isotropic, orthotropic, and as a reference, rigid) translating in calm water and in the presence of regular head waves. Aluminum is chosen as the material for the isotropic hydrofoil. Material properties given by Liao, *et al.* (2019) for a carbon-fiber reinforced polymer structure are utilized in this study for orthotropic hydrofoils, and the fiber orientation angle is considered here as one of the main variable parameters.

## **COMPUTATIONAL APPROACH**

The multiphysics software, SimCenter STAR-CCM+ of version 14.06 was applied in this study. This program includes both a finite element solver and a finite volume CFD solver. The volume-of-fluid (VOF) method with a high-resolution interface capturing scheme was applied for multi-phase representation of air and water flow (Hirt & Nichols, 1981). Since one of the current objectives is to keep simulations computationally efficient, the Reynolds Averaged Navier Stokes (RANS) approach

was utilized for modeling turbulent flow. A two-way coupled fluid-structure interaction technique was used, accounting for mutual interaction between fluid flow and solid structure. At each iteration, the fluid forces on the hydrofoil surface are obtained with the CFD solver, and mapped to the surface of the structural model. Then, displacements of the hydrofoil structure are determined; and these displacements are applied to the fluid grid, which is morphed to accommodate a new shape of the deformed hydrofoil. The hydrodynamic forces are then solved for again and mapped back to the solid model. This process is repeated for each time step in the simulation.

The computational viscous solver with the 2<sup>nd</sup>order convection discretization and the 1st-order implicit stepping in time was employed in this work. For simulations in calm water, only steady-state results were of interest. A time step of 0.1 s and 5 inner iterations per time step were employed. This was sufficient to maintain Courant numbers adequate for the high-resolution interface capturing scheme (HRIC) and allowed fast development of the flow to obtain steady results. The calm-water simulations were run until monitors of the main metrics (lift and drag coefficients, twist, deflection, and maximum stress) converged within 1% over 200 time steps. For unsteady simulations in waves, a timeaccurate model with an adaptive time step was implemented. The target for the time step was chosen to maintain a free-surface Courant number below one, whereas the upper bound for the time step was selected as the wave encounter period divided by 200 and the lower bound was chosen as  $5 \cdot 10^{-4}$  s for practicality. The number of inner iterations was also adapted to ensure that the main metrics converge within 1% over three iterations, with the maximum number of inner iterations being limited by 20. In most situations, the full convergence was achieved at each time step.

The main governing fluid mechanics equations solved numerically by the CFD solver include the continuity, momentum and volume fraction transport equations for the Reynolds-averaged flow properties,

$$\nabla \cdot \boldsymbol{v} = 0 \,, \tag{1}$$

$$\frac{\partial}{\partial t}(\rho v) + \nabla \cdot (\rho v \otimes v) = -\nabla \cdot (PI) + \nabla \cdot (T + T_t) + \mathbf{B},$$
(2)

$$\frac{\partial \beta}{\partial t} + \nabla \cdot (\beta \mathbf{v}) = 0 , \qquad (3)$$

where v is the flow velocity vector,  $\rho$  is the fluid mixture density, P is the pressure, I is the identity tensor, T is the viscous stress tensor,  $T_t$  is the Reynolds stress tensor,  $T_t$  is the body force, and  $\beta$  is for the volume fraction occupied by air. The fluid density  $\rho$  and viscosity  $\mu$  are

determined via air and water properties as  $\rho = \rho_{air}\beta + \rho_{water}(1-\beta)$  and  $\mu = \mu_{air}\beta + \mu_{water}(1-\beta)$ . Constant densities were utilized for air and water. The surface tension was activated in the solver settings. The Reynolds stresses for incompressible flows are modeled as follows,

$$T_t = 2\mu_t S - \frac{2}{3}\rho kI , \qquad (4)$$

where  $\mu_t$  is the turbulent eddy viscosity, S is the mean strain rate tensor, and k is the turbulent kinetic energy.

The realizable two-layer  $k - \varepsilon$  model (Rodi, 1991; Shih, *et al.*, 1995) was employed here, as it proved to perform well in a previous modeling of ventilated hydrofoils (Matveev, *et al.*, 2019). The  $k - \omega$  model was also tried for several validation cases in this study but produced similar results. The governing equations for the turbulent kinetic energy k and the turbulent dissipation rate  $\varepsilon$  in the realizable  $k - \varepsilon$  model are given as follows,

$$\frac{\partial}{\partial t}(\rho k) + \nabla \cdot (\rho k \mathbf{v}) =$$

$$\nabla \cdot \left[ \left( \mu + \frac{\mu_t}{\sigma_k} \right) \nabla k \right] + P_k - \rho \varepsilon ,$$
(5)

$$\frac{\partial}{\partial t}(\rho \varepsilon) + \nabla \cdot (\rho \varepsilon v) = \nabla \cdot \left[ \left( \mu + \frac{\mu_t}{\sigma_{\varepsilon}} \right) \nabla \varepsilon \right] + C_{\varepsilon 1} P_{\varepsilon} \frac{\varepsilon}{k} - \rho C_{\varepsilon 2} \frac{\varepsilon^2}{k + \sqrt{\nu \varepsilon}},$$
(6)

where  $P_k$  and  $P_{\varepsilon}$  are production terms,  $\nu$  is the kinematic viscosity,  $C_{\varepsilon 1}$ ,  $C_{\varepsilon 2}$ ,  $\sigma_k$  and  $\sigma_{\varepsilon}$  are the model coefficients.

For modeling solid mechanics, a finite element solver was applied. The governing equation for the displacement of the body element  $\boldsymbol{u}$  is given as follows,

$$\rho \ddot{\boldsymbol{u}} - \nabla \cdot \boldsymbol{\sigma} - \boldsymbol{F} = 0 , \qquad (7)$$

where F is the body force per unit volume and  $\sigma$  is the Cauchy stress tensor. Using the applied fluid forces, the solid displacements can be determined. Material damping was neglected in this study. Second order hexahedral elements with twenty nodes in each element were used to discretize the hydrofoil structure, and a quadratic shape function was applied to determine the hydrofoil structural motion and deformations.

In order to construct a computationally efficient model for parametric calculations with flexible hydrofoils in waves (the main goal of this study), three regions of numerical mesh were generated in the domain: a background grid in the entire the fluid domain (Figure 2), a fluid grid around a hydrofoil where hydrofoil motions occur (Figure 3), and a solid mesh for the hydrofoil structure (Figure 4), which consisted of 2<sup>nd</sup> order hexahedral elements. The trimmed octree-based

grids with hexahedral cells were built inside fluid regions. Prismatic mesh layers were applied at the hydrofoil surface. The near-wall cell thicknesses were between 30 and 100 of Y+ values (with average values around 50); and thus, wall functions were invoked in the turbulence modeling. The overall numerical domain was 85 foil chords long, 32 chords wide and 18 chords tall. The number of cells in the numerical domain was between one and two million, with more denser grids applied for simulations in wave conditions, where more refined free-surface zones are needed to adequately capture surface waves.

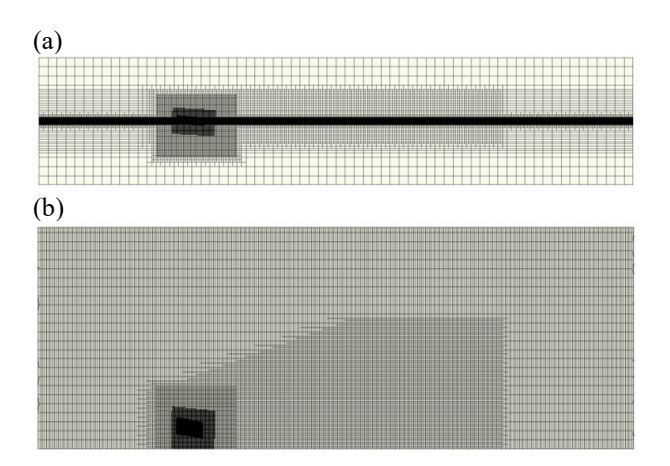
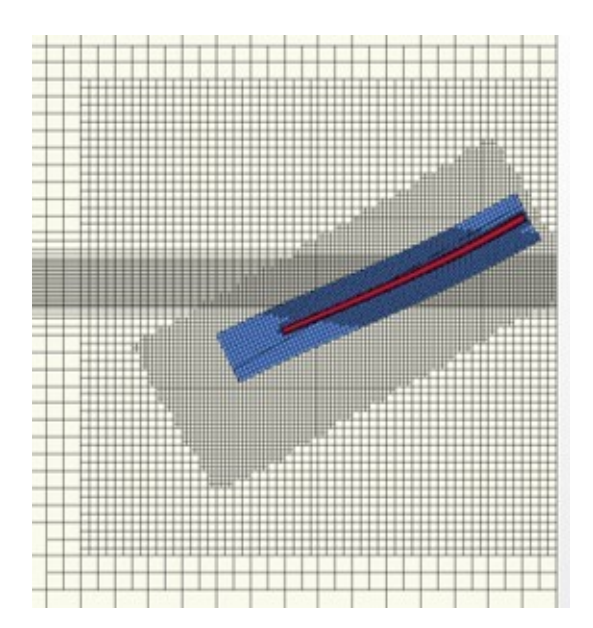


Figure 2: (a) Side vertical-plane view and (b) top horizontal-plane view of background mesh.



**Figure 3:** Front vertical-plane view of overset/morphing mesh (blue) around deformed hydrofoil (red) superimposed on background mesh.

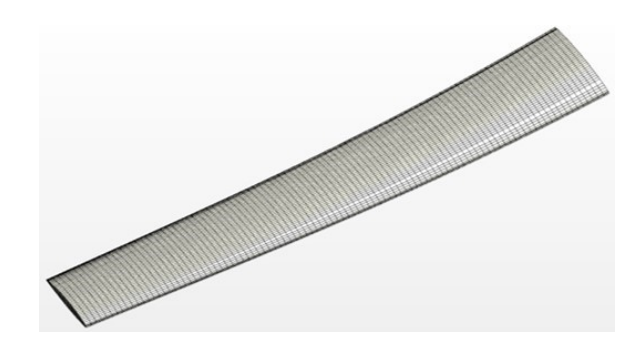


Figure 4: Solid mesh on hydrofoil.

Numerical cells in the background grid come in contact with the near-foil fluid grid at the overset interface, where information is obtained by linear interpolation from both meshes. The hydrofoil surface in the fluid domain communicates with the solid grid via the mapped contact interface. The fluid mesh morphing occurs within the near-hydrofoil region. The advantage of employing two fluid grids is the improved robustness of the simulation. The overset boundary is not fixed and can move freely. This helps generating high-quality mesh during the grid morphing. In addition, the mesh can be aligned with the foil in the secondary region, which reduces probability of appearance of cells with small faces on the hydrofoil surface, thus minimizing a likelihood of creating negative volumes during mesh morphing. Having two fluid grids also allows for the background mesh to be aligned with the fluid flow, which helps capturing gradients in the flow model with smaller mesh count.

The boundary conditions used for flexing foil simulations are illustrated in Figure 5. A symmetry plane is imposed on the hydrofoil port side. The hydrostatic pressure outlet is prescribed on the downstream boundary. The four remaining sides of the numerical domain utilize a velocity inlet corresponding to the assigned calm-water or wave conditions. The numerical wave dampening (in calm water) and forcing (in waves) is used near the downstream and starboard boundaries to suppress numerical wave reflections. The length of the damping zone equals to about 10 mean chords of a hydrofoil. In the wave simulations, the forcing zone size is 1.5 of the incident-flow wavelength at the downstream boundary and 1 of the wavelength at the starboard boundary. For modeling head waves, the 5th order Stokes wave model is used at the inlet and forcing zones.

The computational time required to simulate one second of physical time of the studied hydrofoils is estimated to be about 300 CPU hours, defined as the actual computational time multiplied by the number of employed processors (Intel Xeon Gold 6130 @ 2.10 GHz).

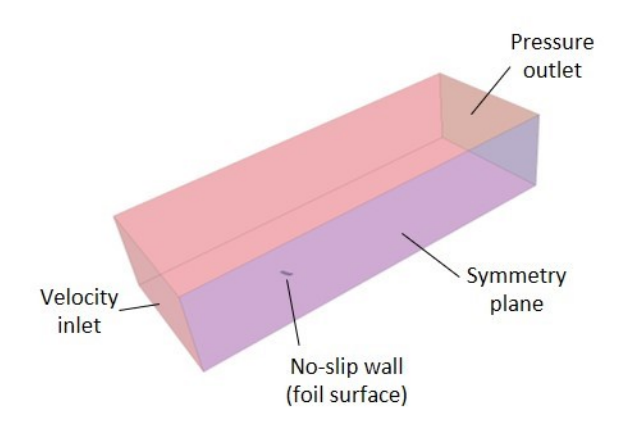


Figure 5: Boundary conditions.

#### VERIFICATION AND VALIDATION

A flexible hydrofoil tested in a water tunnel by Ducoin, et al. (2009) was used in the present study for verification and validation of the computational approach. In addition, a comparison between current numerical results and previous experimental data was also made for a flexible vertically-oriented hydrofoil studied by Harwood (2016).

The rectangular hydrofoil investigated by Ducoin, *et al.* (2009) had a section based on NACA66 family with camber-to-chord ratio 2%, thickness-to-chord ratio 12%, chord 150 mm, and span 191 mm. The hydrofoil was made of POM polyacetate material with properties listed in Table 1. The hydrofoil was placed horizontally in the single-phase water flow inside the water tunnel with a square section of width 192 mm, which is just slightly wider than the hydrofoil span. The hydrofoil root was fixed on one of the channel walls, while the tip section was free. The investigated case involved the incident water flow velocity 10 m/s and the hydrofoil pre-set attack angle of 6 degrees.

**Table 1:** Material properties of hydrofoil tested by Ducoin, *et al.* (2009).

Density	$1480 \text{ kg/m}^3$
Young's modulus	3 GPa
Poisson's ratio	0.35

Three numerical grids (coarse, medium, and fine) were constructed in a way that cell dimensions were refined with a factor of  $\sqrt{2}$  between coarse/medium and medium/fine grids. The overall cell counts in these grids were 0.39, 0.66 and 1.23 million. Illustrations of the mesh and calculated hydrofoil displacements are shown in Figures 6 and 7, respectively. In Figure 6, a small gap between the hydrofoil free tip and the channel wall can

be noticed on the right side, while the hydrofoil root is fixed on the opposite wall. The maximum tip deflection and twist in the tip section reported in the experiments were used as the metrics for the mesh-convergence studies.



**Figure 6:** Front view on fine mesh in the fluid domain around deformed hydrofoil in V&V study.

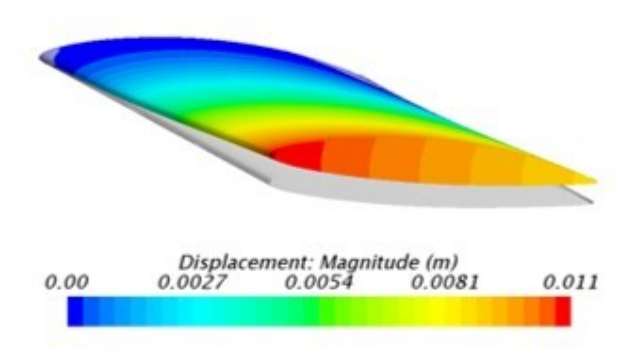


**Figure 7:** Hydrofoil displacements obtained on fine grid. Grey volume shows original (non-deformed) hydrofoil shape.

The computational and test results, as well as calculations from the numerical uncertainty analysis, are summarized in Table 2. The Richardson extrapolation was used for the expected correction  $\delta_{RE}$  to the solution obtained on the fine mesh (Ferziger & Peric, 1999),

$$\delta_{RE} = \frac{\Delta_{21}}{2^p o b - 1},\tag{8}$$

where  $\Delta_{21}$  is the difference between solutions found on the fine and medium grids, and  $p_{ob}$  is the observed order of accuracy,

$$p_{ob} = \frac{\log \left(\Delta_{23}/\Delta_{12}\right)}{\log \left(\beta\right)},\tag{9}$$

where  $\Delta_{23}$  is the difference between solutions on the medium and coarse mesh, and  $\beta$  is the ratio of numerical cell dimensions, being  $\sqrt{2}$  in this study. Then, the factor of safety F was applied to determine the grid-based simulation uncertainty as  $U_{NS} = F | \delta_{RE} |$  (Xing & Stern, 2010). Finally, the validation uncertainty was estimated as follows,

$$U_V = \sqrt{|U_D|^2 + |U_{NS}|^2} \,, \tag{10}$$

where  $U_D$  is the experimental uncertainty, evaluated from information given by Ducoin, *et al.* (2009). Since the validation uncertainties were found to be greater than the differences between numerical and test results (Table 2), the present numerical approach is considered as validated for this case. In the subsequent simulations, similar solver settings and mesh properties were implemented.

**Table 2:** Data for tip deflection and twist and results of numerical uncertainty analysis. Validation is assessed by comparing characteristics shown in bold.

	Maximum tip	Twist at
	deflection	the tip
Numerical values on	10.8 mm	$0.829^{\circ}$
fine mesh, $y_{num}$		
Numerical uncertainty,	0.13 mm	$0.0005^{\circ}$
$U_{NS}$		
Exper. uncertainty, $U_D$	0.4 mm	0.178°
Validation	0.42 mm	0.178°
uncertainty, $U_V$		
Experimental values,	~10.8 mm	0.81°
$y_{exp}$		
Difference between	< 0.1 mm	< 0.02°
values, $ y_{num} - y_{exp} $		

The second validation case was based on a vertically oriented flexible hydrofoil from the experimental series of Harwood (2016). This hydrofoil (or strut) had a symmetric profile with a blunt trailing edge and the following parameters: chord 279 mm, thickness 28 mm, and span 910 mm. At the condition selected for validation, the foil submergence was 279 mm, initial attack angle 12.5°, and water speed 5.88 m/s, corresponding to the chord-based Froude number of 3.55. The hydrofoil was made of Type I PVC material

and was equipped with spars for measuring tip deflection and twist.

The computationally simulated hydrofoil displacements and water surfaces in the steady state are shown in Figure 8. One can notice a ventilated base of the hydrofoil, but the two lateral sides were primarily wetted in this condition. The hydrodynamic results from the tests were presented in the form of the lift and drag coefficients, using the submerged planform area for reference, and the moment coefficient about the midchord axis. The numerically obtained hydrodynamic and structural parameters, as well as experimental data, are given in Table 3. The agreement between numerical and test results is considered satisfactory.

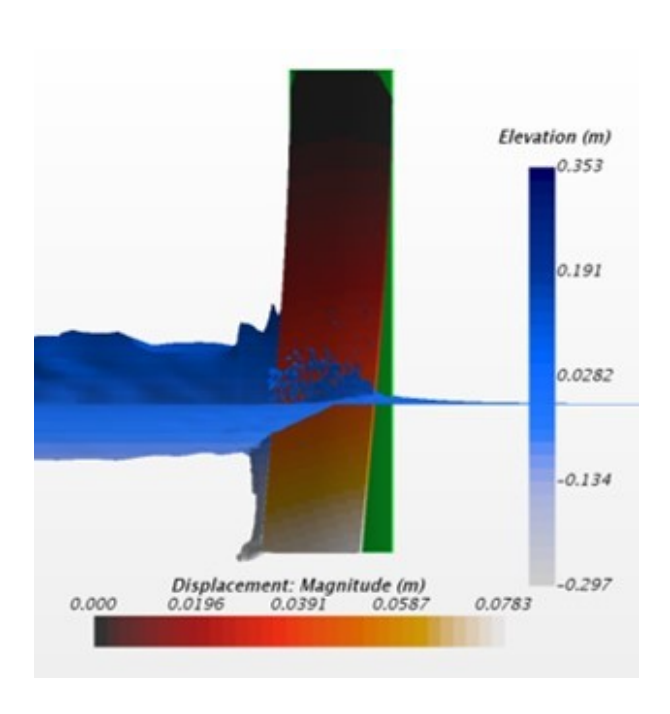


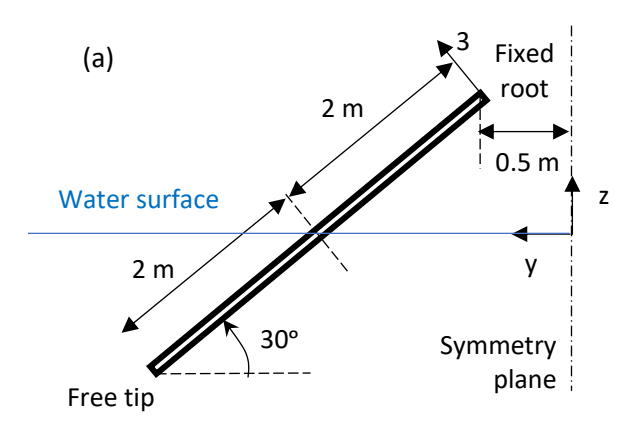
**Figure 8:** Structural displacements and free water surface elevations around vertical hydrofoil. Original (non-deformed) hydrofoil shape is shown in green.

**Table 3:** Comparison of experimental and computational results for vertical surface-piercing hydrofoil.

	Test data	Numerical results
Lift coefficient	0.363	0.380
Drag coefficient	0.10	0.081
Moment coefficient	0.108	0.110
Tip deflection	77 mm	78 mm
Twist at the tip section	1.48°	1.34°

# CONDITIONS USED IN PARAMETRIC STUDY

For parametric simulations of surface-piercing dihedral hydrofoils with different material properties, an inclined tapered hydrofoil with a fixed root above water and a free tip under water is considered in this study. The hydrofoil schematic with main dimensions is shown in Figure 9, with x-axis oriented along the flow and z-axis in the vertical direction. The same hydrofoil profile (based on NACA66 family) as in the above verification and validation study is used for the surface-piercing hydrofoil simulations. The symmetry plane near the fixed root implies that this setup is similar to an inverse-V foil configuration. In all cases of the parametric study cases, the attack angle of the undeformed hydrofoil was 3 degrees and its forward speed was set to 8 m/s.



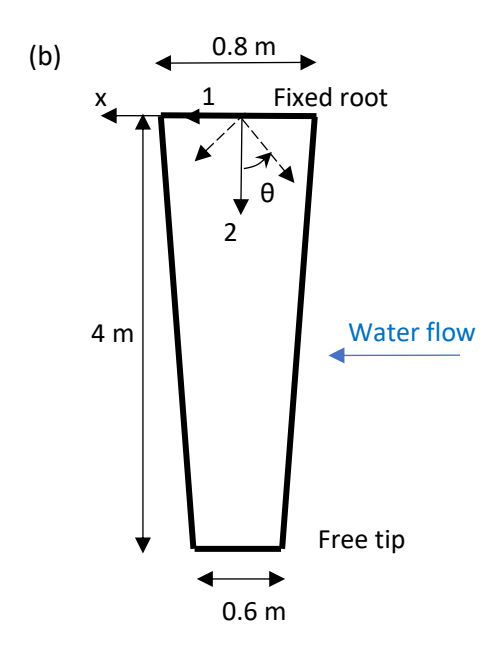


**Figure 9:** Schematic of surface-piercing hydrofoil (not to scale): (a) front view, (b) platform view.

Two incident water flow conditions were analyzed, one being calm water and the other having regular head waves of height 0.6 m and wavelength 18 m which is representative of Sea State 3.

Several types of structural properties were employed in these simulations. One was a perfectly rigid foil used as a reference for comparison. The second was an aluminum hydrofoil with isotropic properties given in Table 4. Then, an orthotropic structure was considered that had different elastic properties in planes perpendicular to each other. The material properties for this hydrofoil were taken from the study by Liao, et al. (2019) of a composite hydrofoil made of carbon-fiber reinforced polymer (CFRP). These properties are listed in Table 5. The stiffest direction along fibers in the planform plane is designated as axis 2 in Figure 9(b). Axis 1 is also in the planform plane, while axis 3 is normal to that plane (Figure 9(a)). The orientation of axis 2 is characterized by angle  $\theta$  (Figure 9(b)). The zero value of this angle means that the fibers are aligned in the spanwise direction. In a hydrofoil with  $\theta$  between  $0^{\circ}$ and 90°, fibers originating at the root are directed toward the hydrofoil leading edge. For  $0^{\circ} > \theta > -90^{\circ}$ , fibers from the root are oriented toward the trailing edge.

**Table 4:** Material properties of aluminum hydrofoil.

Density	$2702 \text{ kg/m}^3$
Young's modulus	68 GPa
Poisson's ratio	0.33

**Table 5:** Material properties of orthotropic hydrofoil.

Density	$1540 \text{ kg/m}^3$
Young's modulus, $E_1$	13.4GPa
Young's modulus, $E_2$	117.8 GPa
Young's modulus, $E_3$	9.4 GPa
Shear modulus, $G_{12}$ , $G_{23}$	3.9 GPa
Shear modulus, $G_{13}$	3.3 GPa
Poisson's ratio, $v_{12}$ , $v_{23}$	0.25
Poisson's ratio, $v_{13}$	0.45

## RESULTS OF PARAMETRIC STUDY

The primary characteristics of hydrofoils obtained in the present simulations in calm water included the lift coefficient, lift-drag ratio, average displacement and twist of the free tip, maximum Von Mises stress and the maximum failure index. The reference area used in the lift coefficient is defined as the projected to the horizontal plane planform area of the hydrofoil portion submerged in water at rest condition. For the failure

index of the composite hydrofoil, a maximum between the matrix tensile/compressive cracking criterion (Hashin, 1980) and the delamination in tension/compression criterion (Ye, 1988) was employed, similar to the metrics used by Liao, *et al.* (2019). Failure index of one or greater would indicate material failure.

The calm-water results are presented in Figures 10-12 for the rigid, aluminum and orthotropic hydrofoil with the fiber orientation angle ranging between -45° to +45°. The lift coefficients for the perfectly rigid foil, aluminum foil and CFRP foil with  $\theta = 0^{\circ}$  are close to each other (Figure 10(a)), since the twist and deflection of CFRP hydrofoil are small at this fiber angle (Figure 11). With fibers oriented toward the leading edge ( $\theta >$ 0°), the orthotropic hydrofoil lift decreases (Figure 10(a)). This is partly caused by negative twist angles at these  $\theta$  (Figure 11(a)). The tip displacement influence is two-fold. First, it reduces the foil dihedral angle, thus increasing the lift. On the other hand, the deflected foil area submerged in water becomes smaller, thus contributing to the lift loss. The tip displacement itself depends on the lift force and fiber orientations (increases with  $\theta$  moving away from 0°), so the hydrodynamic characteristics and structural deformations become nonlinearly interdependent. In cases with negative  $\theta$ , the lift coefficient is higher (Figure 10(a)), since significant positive twist angles effectively increase the foil attack angle (Figure 11(a)), and even larger foil deflection is insufficient to suppress this trend. The maximum and minimum lift coefficients are achieved at -25° and +30° fiber angles, respectively.

The dependence of the lift-drag ratio of the orthotropic hydrofoil on the fiber orientation angle is non-monotonic (Figure 10(b)). It has a maximum near  $\theta = 0^{\circ}$ , decreases with deviation of  $\theta$  from  $0^{\circ}$ , and then grows again at large magnitudes of the fiber angle. The twist behavior (Figure 11(a)) changes similarly to the lift coefficient (Figure 10(a)), implying a strong twist-lift correlation. The tip displacement increases with the fiber angle deviating from the spanwise direction, which makes the foil more prone to deflection due to reduced bending rigidity. The maximum values of the stresses and the failure index are given in Figure 12. With fibers directed toward the trailing edge ( $\theta < 0^{\circ}$ ), these metrics correlate well with lift coefficient, whereas at  $\theta > 0^{\circ}$  they decrease only up to  $\theta = 10^{\circ}$  and then start growing.

The dependence of hydrodynamic properties of orthotropic foils on the fiber orientation can be utilized in the design process of a foil-assisted boat. If reducing variations of the foil lift force over a broad speed range is a priority, positive  $\theta$  would be beneficial, since the corresponding lift coefficient becomes smaller at higher load that increases with speed. On the other hand, if minimal foil drag is desirable at low speeds (in the displacement regime of a boat), but high lift is needed at high speeds (in the boat's foilborne regime), then

negative  $\theta$  on a foil with a small installed attack angle would be preferable.

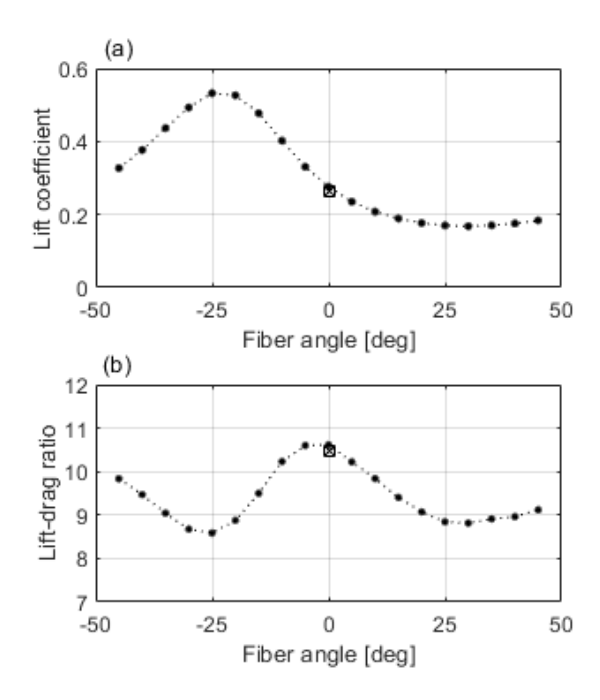


**Figure 10:** (a) Lift coefficient and (b) lift-drag ratio for orthotropic foil (dots connected with dotted line), aluminum foil (square) and rigid foil (crosses).

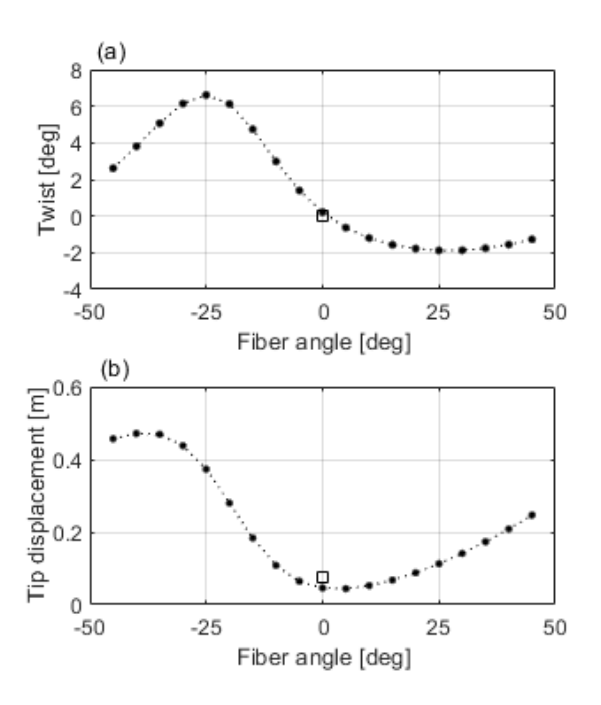


Figure 11: (a) Twist and (b) displacement at the tip for orthotropic foil (circles connected with dotted line) and aluminum foil (square).

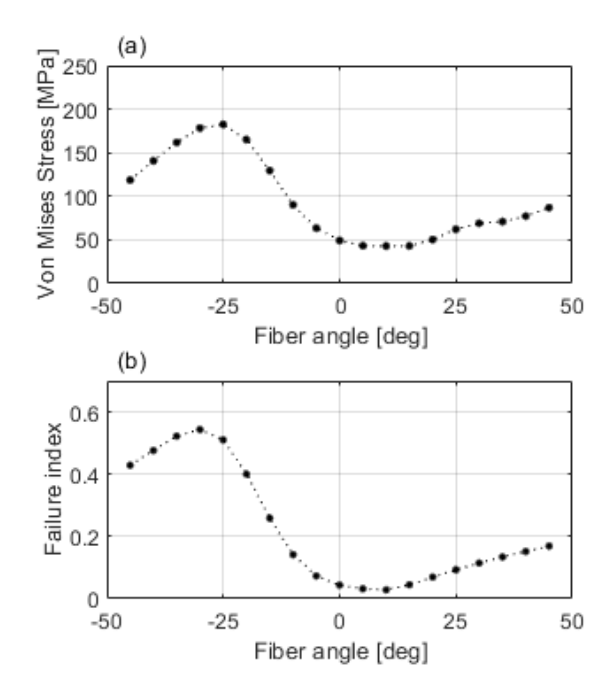
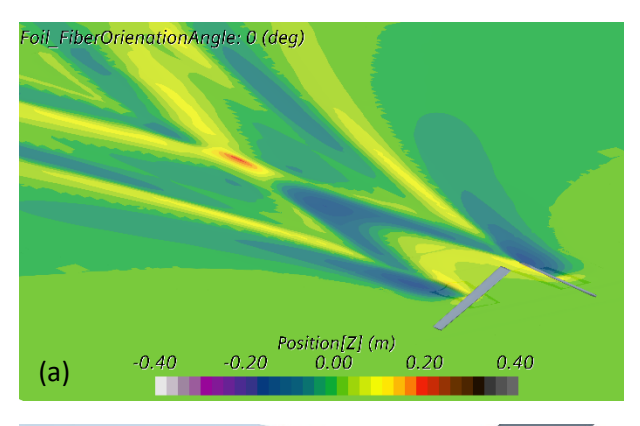


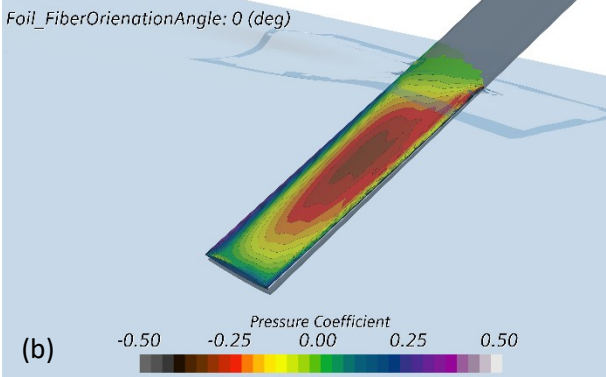
Figure 12: Maximum values for (a) Von Mises stress and (b) failure index for orthotropic foil (circles connected with dotted line) and aluminum foil (square).

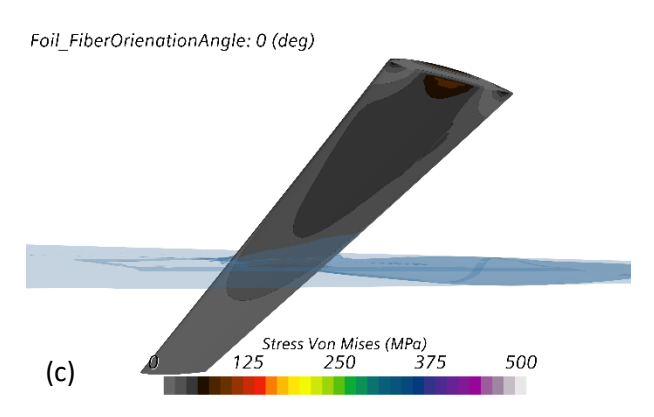
The illustrations of water surface deformations, pressure coefficients on the suction (upper) side, and stresses on the pressure (lower) side for three orthotropic hydrofoils ( $\theta=0^{\circ}$ , -45°, +45°) are shown in Figures 13-15. The lower foil images in sub-figures (a) and (b) indicate the original (non-deformed) hydrofoil shapes. The water surfaces around the rigid and aluminum hydrofoils (not shown) were similar to those near the composite hydrofoil with  $\theta=0^{\circ}$ , consistent with relatively small differences in other characteristics (Figures 10-11). The water elevations are presented together with the symmetry image, since modeling of a single hydrofoil with a symmetry condition near its fixed root (Figure 9(a)) produces water deformations equivalent to those around an inverse-V foil system.

The wave patterns of three orthotropic hydrofoils have several similar features. The water depressions are located behind individual foils, similar to a wave hollow formed behind a planing hull. In addition, there is another pronounced water depression located at some distance behind hydrofoils near the symmetry plane. This wave hollow is formed by actions of both foils. A significant water elevation ("rooster tail") following this water hollow is also typical to wave patterns behind fast boats. A system of divergent waves is present further downstream. Water spray can be noticed on the foil suction sides near their intersections with the water free surface. The spray, as well as

magnitudes of water deformations, is most pronounced for the hydrofoil with fiber angle -45° (Figure 14(a)), which experiences the largest deflection among the three hydrofoils (Figure 14(b)).



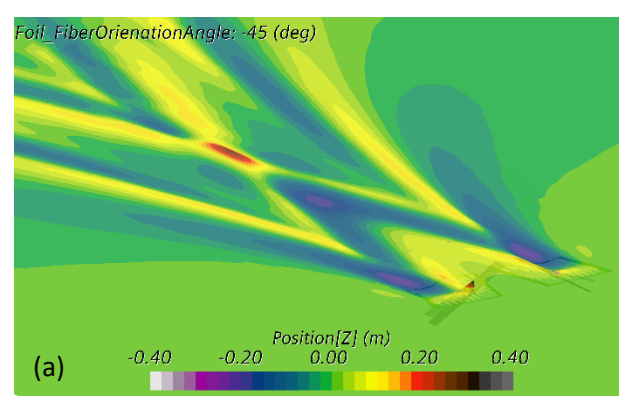


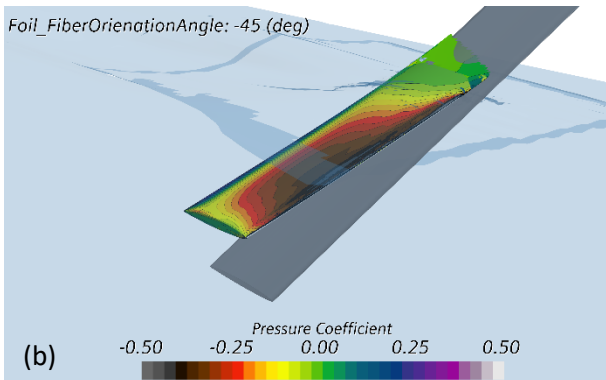


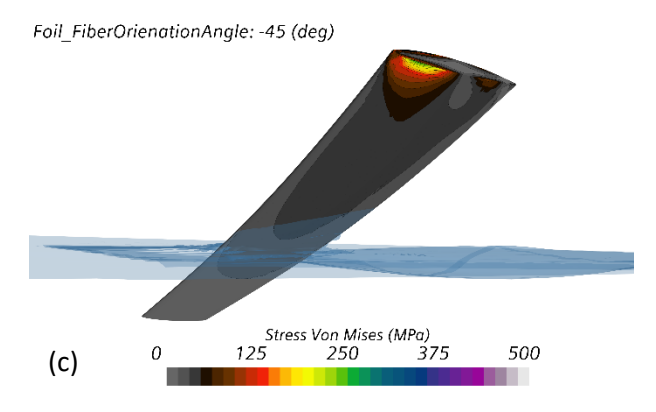
**Figure 13:** Orthotropic hydrofoil with fiber angle  $0^{\circ}$  in calm water: (a) water surface elevations; (b) pressure coefficient on the foil suction side; (c) Von Mises stress on the foil pressure side.

The pressure coefficients on the suction sides reach minimum (negative) values near the centers of the submerged sections and closer to the leading edge in case of the foil with  $\theta = -45^{\circ}$  (Figure 14(b)). The (negative) pressure magnitudes are smallest for the foil with  $\theta = -45^{\circ}$  (Figure 14(b)).

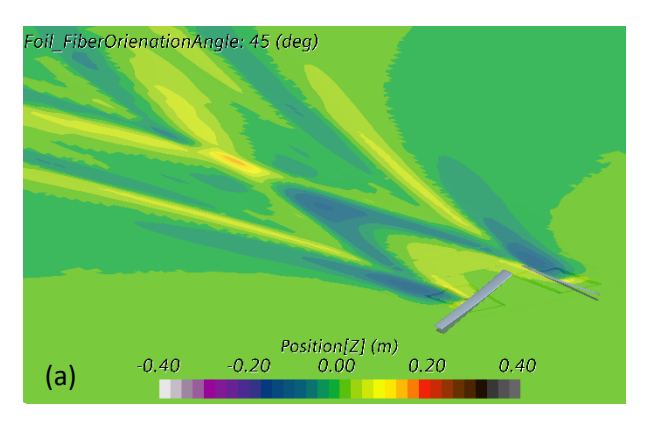
+45° (Figure 15(b)), consistent with its lowest lift coefficient (Figure 10(a)) among the three hydrofoils. The stresses on the foil pressure side reach maxima at the fixed root. For the foil with spanwise fibers (Figure 13(c)), the maximum stress point is near the mid-chord, whereas for other fiber orientations, the stress maxima shift toward the leading or trailing edges (Figures 12(c), 14(c)). The maximum stress values are reached on the foil with  $\theta = -45^{\circ}$ , while the minimum stresses are present on the foil with  $\theta = 0^{\circ}$ , consistent with the twist and bending deformations (Figure 11).

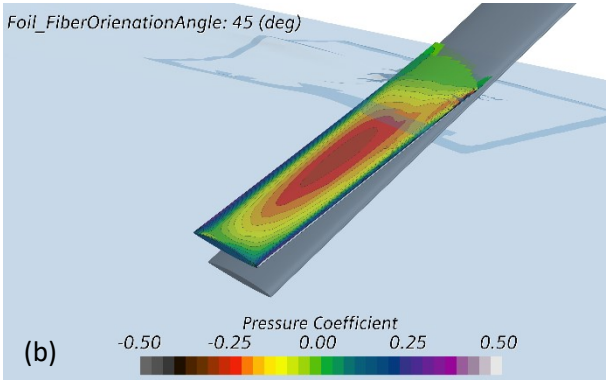






**Figure 14:** Orthotropic hydrofoil with fiber angle -45° in calm water: (a) water surface elevations; (b) pressure coefficient on the foil suction side; (c) Von Mises stress on the foil pressure side.





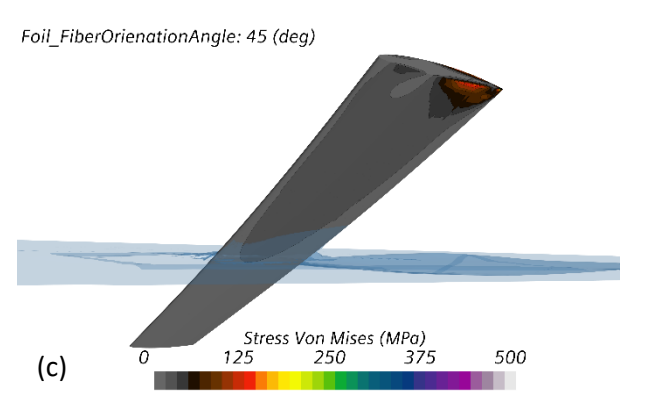


**Figure 15:** Orthotropic hydrofoil with fiber angle +45° in calm water: (a) water surface elevations; (b) pressure coefficient on the foil suction side; (c) Von Mises stress on the foil pressure side.

The second set of parametric simulations was carried out in this study for hydrofoils in the regular head wave conditions. The simulations were run until repeatable in time responses were established. Data obtained in two steady-state cycles for selected hydrodynamic and structural characteristics of the rigid, aluminum and three orthotropic hydrofoils (with  $\theta$  = -45°, 0°, +45°) are presented in Figures 16-19. Also depicted in these figures (by the dotted line) is the scaled water surface elevation that would be present at the

location of the hydrofoil leading edge in the absence of hydrofoil influence. This water elevation is scaled and shifted in magnitude to fit the variation ranges of the shown foil characteristics, but its time dependence is not altered. The actual amplitude of the incident waves was 0.3 m in all simulations with waves.

As one can see in Figure 16, the rigid, aluminum and one of composite foils (with the spanwise fiber orientation) produce similar, near-sinusoidal

responses. The lift characteristics of these hydrofoils were also similar in calm water (Figure 10(a)). The peaks of the lift forces in wave conditions slightly lead the water surface elevation (Figure 16). Thus, the maximum lift forces are generated when these hydrofoils experience large submergence in the incident wave. The flexible foils (aluminum and CFRP) have peaks of lift coefficients occurring slightly later than that of the rigid foil.

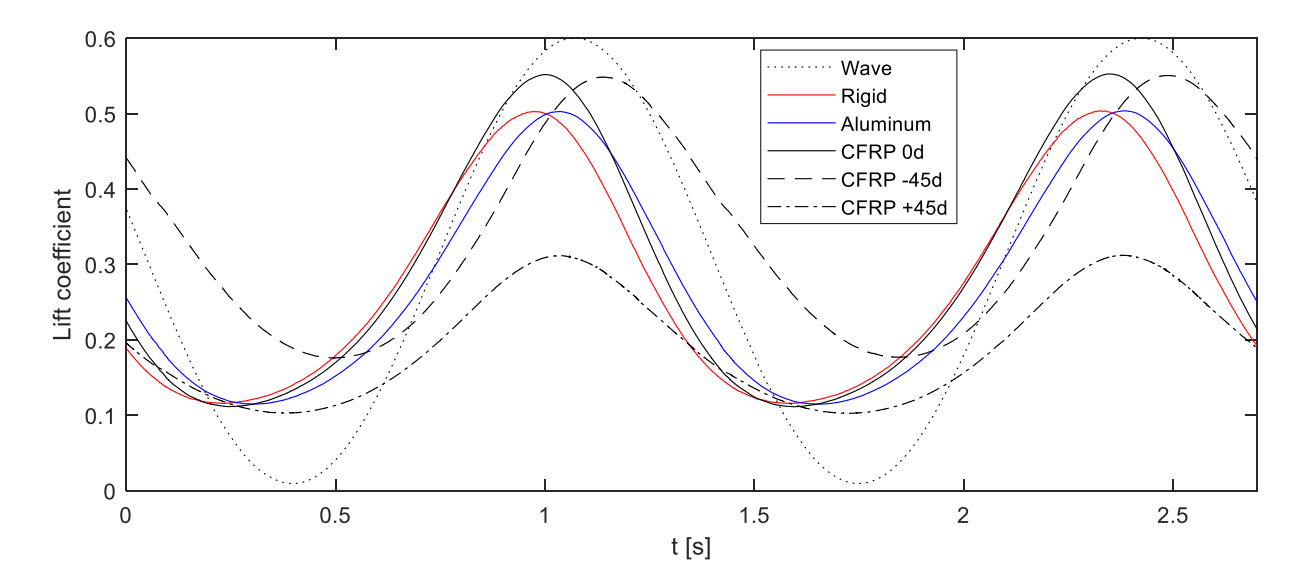


**Figure 16:** Lift coefficient of hydrofoils in waves in repeatable regime. Dotted line represents scaled water surface elevation of the incident wave.

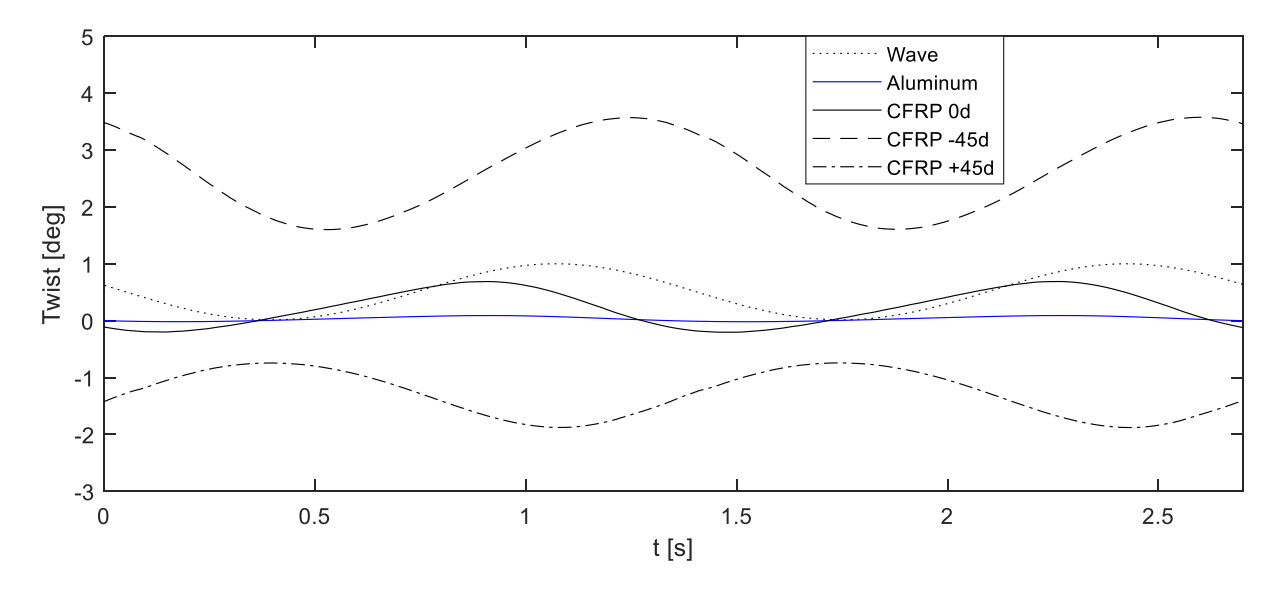


Figure 17: Tip twist of flexible hydrofoils in waves. Dotted line represents scaled water surface elevation of the incident wave.

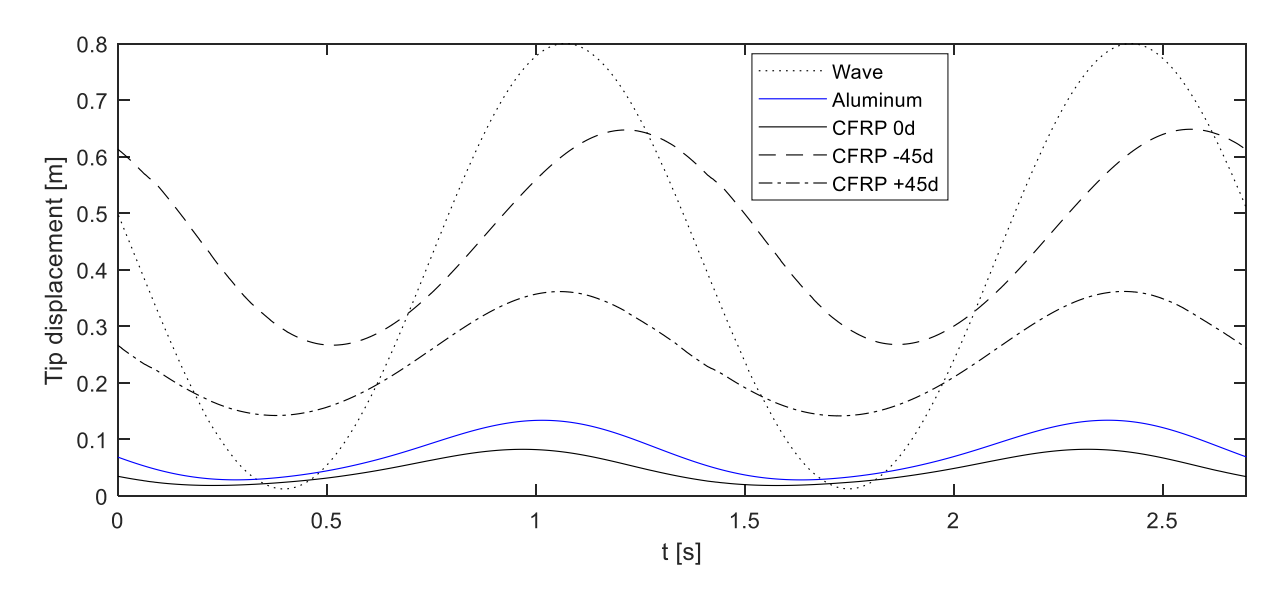
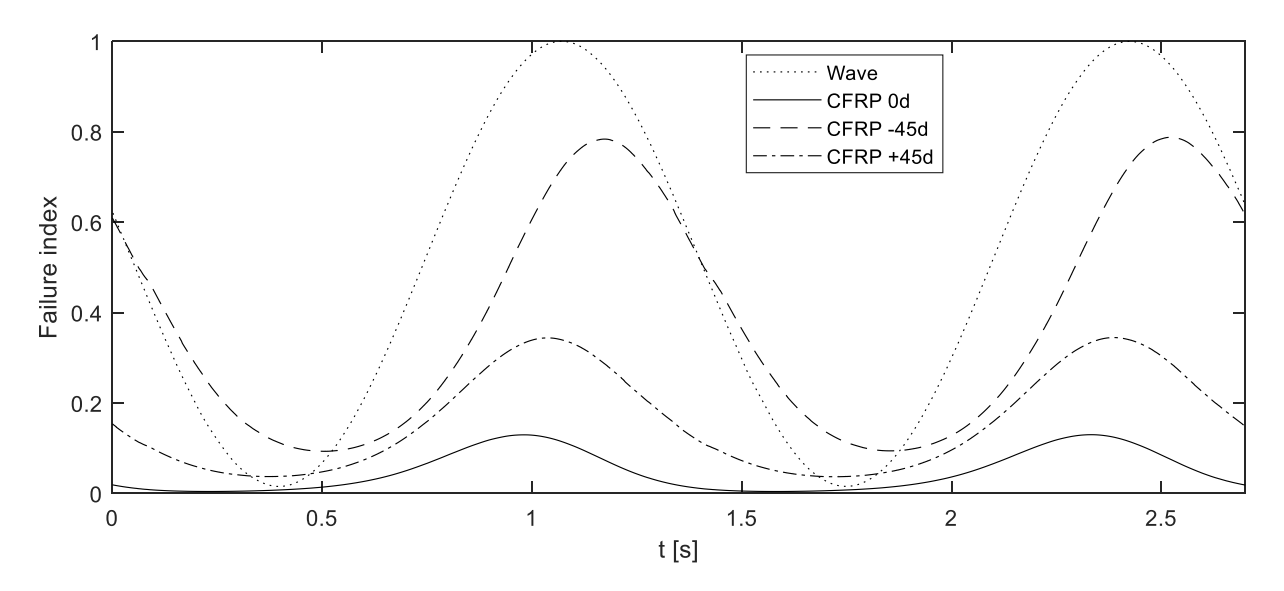


Figure 18: Tip displacement of flexible hydrofoils in waves. Dotted line represents scaled water surface elevation of the incident wave.



**Figure 19:** Failure index of composite hydrofoils in waves. Dotted line represents scaled water surface elevation of the incident wave.

The lift oscillation magnitude of more flexible CFRP foil is slightly larger than that of the aluminum foil. The mean value and fluctuation amplitudes of the lift coefficient of the orthotropic foil with fibers leaning towards the leading edge ( $\theta = +45^{\circ}$ ) are substantially smaller, again similar to the difference in calm water and due to smaller twist angles. The lift coefficient of the composite hydrofoil with negative  $\theta$  slightly lags the wave elevation, while its mean value is bigger.

The twist of the aluminum hydrofoil is close to zero (Figure 17), whereas its tip deflection oscillations are rather modest (Figure 18). The CFRP hydrofoil with spanwise fibers exhibits larger twist fluctuations, but smaller tip motions, consistent with calm-water results. The composite hydrofoils with non-zero  $\theta$  demonstrate larger oscillation magnitudes of both twist and tip deflection, especially for the foil with fibers directed toward the trailing edge. There are larger variations of phase shifts for the twist, whereas phases of the tip

displacements are similar to those of the lift coefficients. The twist oscillations of the foil with  $\theta = +45^{\circ}$  are almost out of phase with the water surface elevations, in contrast to the other foils.

The failure indexes of the orthotropic foils are shown in Figure 19. Their variations in time are correlated with the lift coefficients (Figure 16). For the CFRP foil with the spanwise fiber orientation, this index remains rather small. For the foil with  $\theta = -45^{\circ}$  that exhibits larger mean lift force, twist amplitudes and tip motions, this index approaches dangerously high levels at moments of large submergence in the wave.

The illustrations of water surface deformations, pressure coefficients on the suction side, and stresses on the pressure side for three orthotropic hydrofoils ( $\theta=0^{\circ}$ , -45°, +45°), when they pass through the wave peaks and troughs, are shown in Figures 20-22. The lower foil images in sub-figures (a) and (b) indicate the original hydrofoil shapes. At these time moments, the foil hydroelastic characteristics generally exhibit large deviations from their mean values (Figures 16-19). Again, the water surfaces around the rigid and aluminum hydrofoils are not shown, but they were similar to those around the composite hydrofoil with  $\theta=0^{\circ}$ .

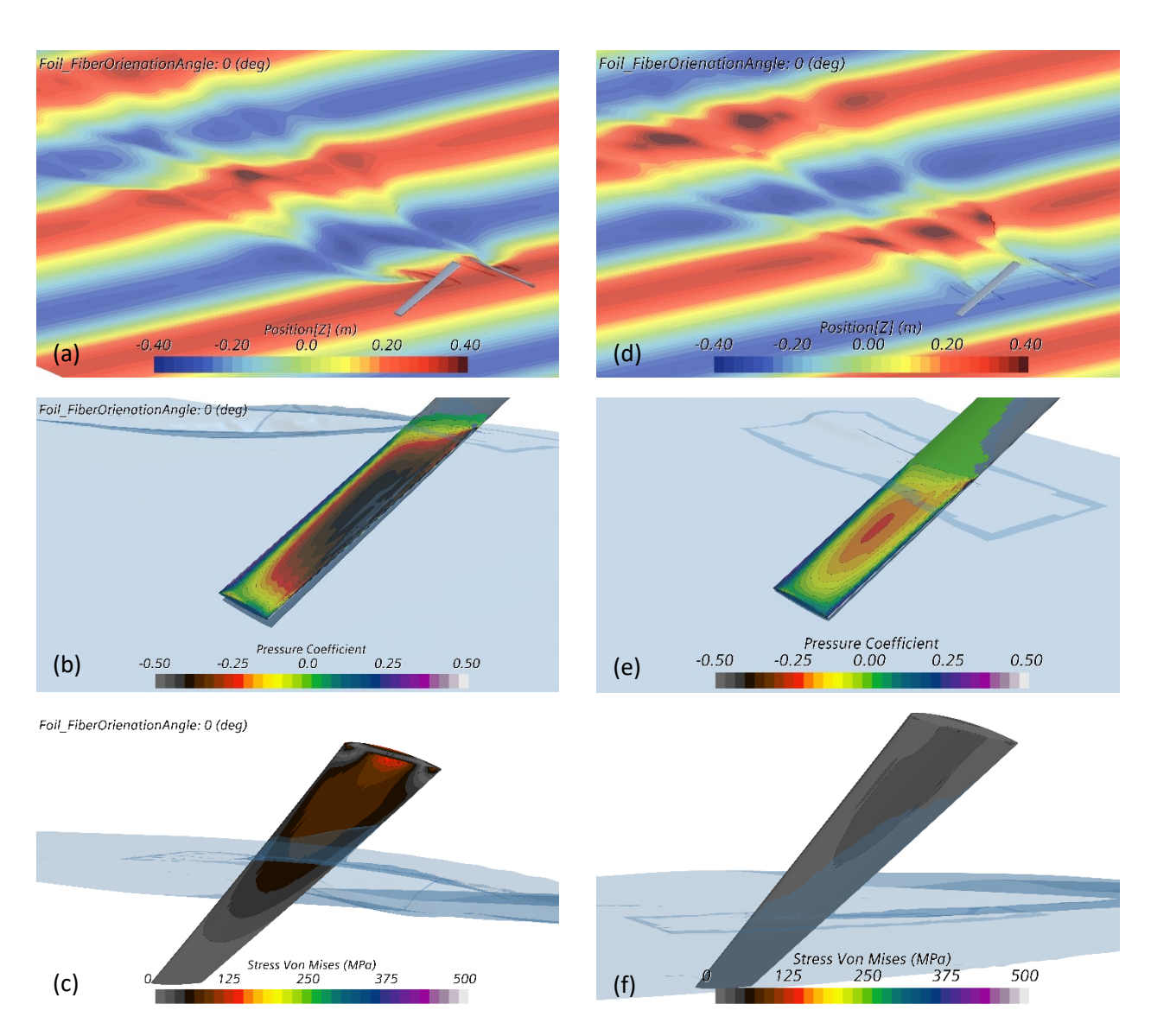


**Figure 20:** Orthotropic hydrofoil with fiber angle 0° passing through (a-c) wave crest and (d-f) wave trough. (a,d) Water surface elevations; (b,e) pressure coefficient on the foil suction side; (c,f) Von Mises stress on the foil pressure side.

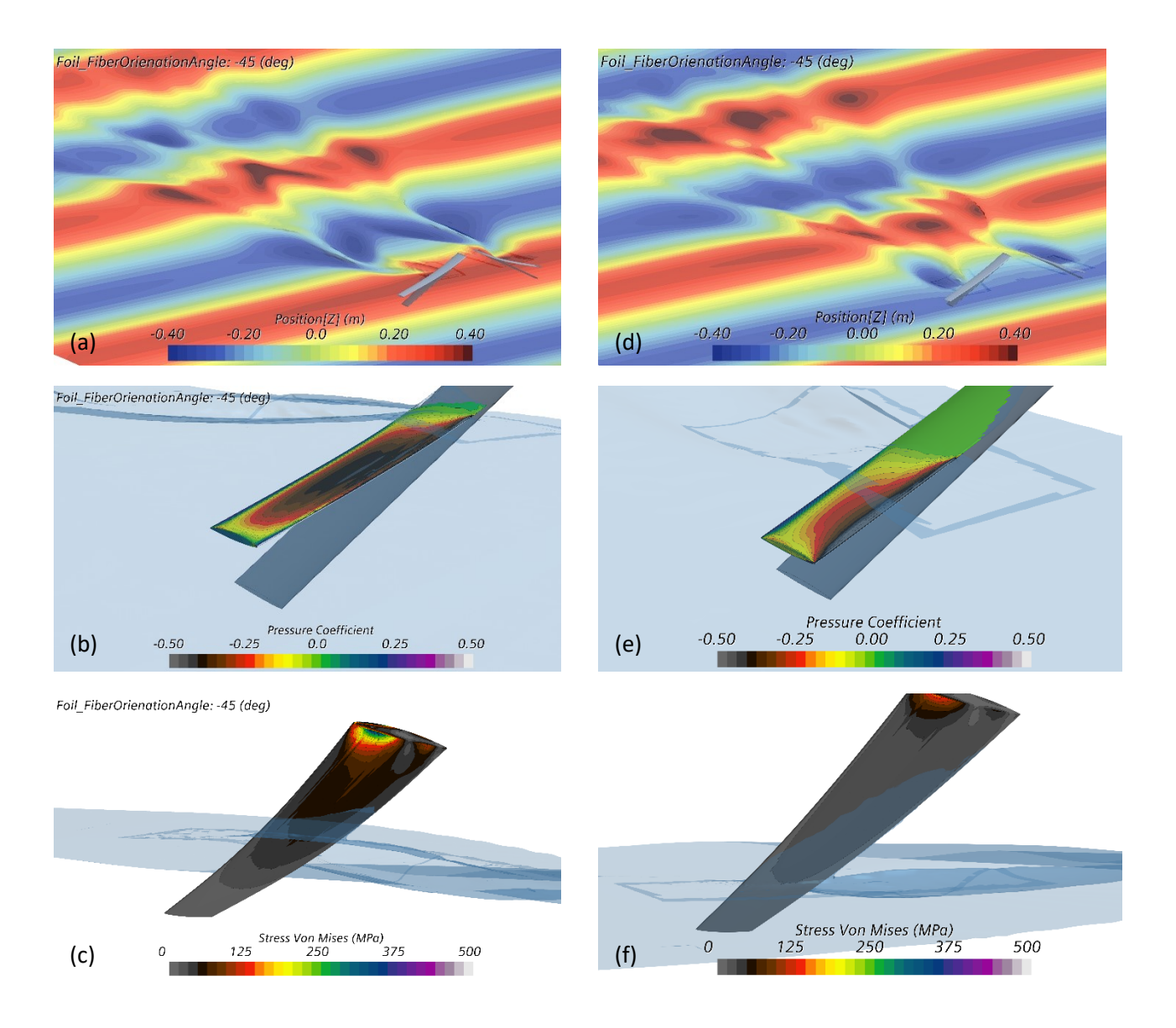


**Figure 21:** Orthotropic hydrofoil with fiber angle -45° passing through (a-c) wave crest and (d-f) wave trough. (a,d) Water surface elevations; (b,e) pressure coefficient on the foil suction side; (c,f) Von Mises stress on the foil pressure side.

The water surface disturbances caused by orthotropic hydrofoils are most pronounced for  $\theta$  = -45° case and least pronounced for  $\theta$  = +45° (Figures 20-22), as in calm-water situations (Figures 13-15). When hydrofoils pass through wave peaks, the wave hollows behind individual foils are displaced further downstream, and the combined wave hollow near the symmetry plane nearly disappears due to a superimposed incident wave pattern at this moment. The tip displacements, pressure coefficient magnitudes, wet surface areas and stresses of hydrofoils crossing wave peaks are visibly larger than those characteristics in calm water. At the moments when hydrofoils are in the wave

troughs, the foil deformations and stresses become smaller.

# **CONCLUSIONS**

High-fidelity computational simulations have been carried out for surface-piercing rigid, isotropic and orthotropic hydrofoils in calm water and in regular head waves. The verification and validations studies were conducted using experimental data reported in the literature for flexible hydrofoils. The hydrodynamic characteristics of an CFRP foil with the fiber direction along the span appeared to be similar to those of an

isotropic aluminum foil and a rigid foil in the studied conditions. However, strong dependence of hydroelastic characteristics of orthotropic foils on the fiber orientation was found. Lift coefficients and twist were generally larger for the foils with fibers directed toward the foil trailing edges and decreased for the foils with fibers leaning toward the leading edges. Both bending and stress magnitudes usually increased for fiber orientations deviating from the span-wise direction, and more pronounced values corresponded to setups with fibers going toward the foil trailing edges. In the absence of waves, the associated water surface deformations showed deep wave hollows behind two symmetrically positioned foils and another hollow near the symmetry

plane further downstream, which was followed by a localized water surface elevation.

Selecting appropriate fiber orientations for composite hydrofoils can provide means for self-regulation of the foil hydrodynamics. For example, composite hydrofoils that produce negative twist under hydrodynamic load would have lower lift coefficients at higher speeds, thus resulting in smaller variations of the lift force in a range of speeds. In contrast, hydrofoils exhibiting positive twist with increasing speed, would lead to larger variations of hydrodynamic forces, which could be used for minimizing foil drag at low speeds, while maximizing foil lift at high speeds.

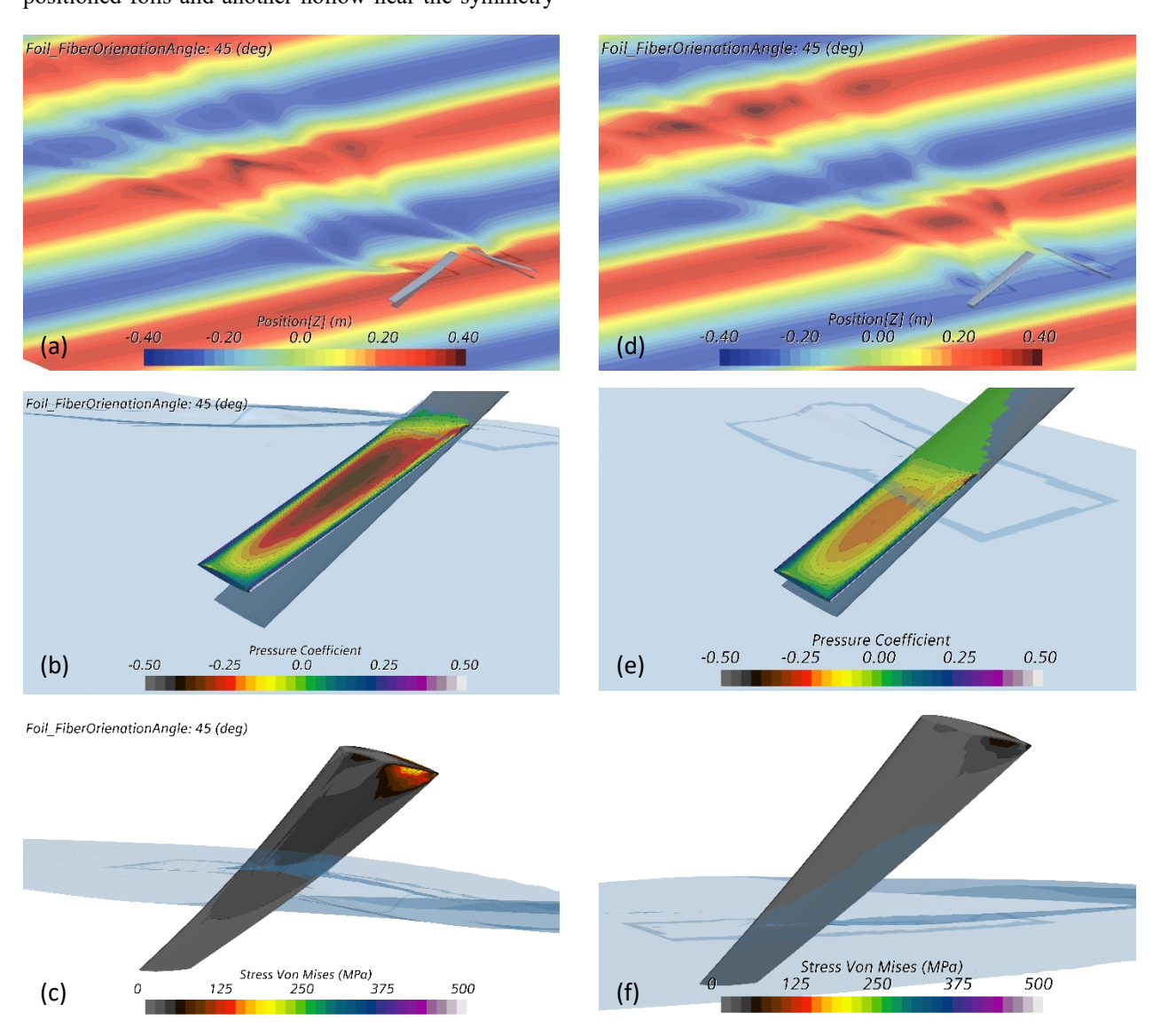


**Figure 22:** Orthotropic hydrofoil with fiber angle +45° passing through (a-c) wave crest and (d-f) wave trough. (a,d) Water surface elevations; (b,e) pressure coefficient on the foil suction side; (c,f) Von Mises stress on the foil pressure side.

In the simulated regular head wave conditions, hydroelastic responses of low-attack-angle hydrofoils demonstrated near sinusoidal behavior. The rigid and isotropic foils exhibited lift force responses similar to those of the orthotropic foil with the spanwise fiber orientation. The maximum lift forces occurred in the periods of large foil submergence, when hydrofoils passed through the wave crests. The orthotropic foils with significant deviations of fiber angles from the spanwise orientation showed smaller lift oscillations but larger twist and bending amplitudes, thus suggesting enhanced hydroelastic damping of such foils. These hydrofoils also exhibited larger values of the failure index, but still below the level of likely failure occurrence in the studied conditions.

### **ACKNOWLEDGEMENTS**

This material is based upon research supported in part by the U.S. Office of Naval Research under Grant No. N00014-17-1-2553 and in part by the National Science Foundation under Grant No. 1800135.

### REFERENCES

Acosta, A.J., "Hydrofoils and hydrofoil craft," <u>Annual Review of Fluid Mechanics</u>, Vol. 5, 1973, pp. 161-184.

Akcabay, D.T. and Young, Y.L., "Parametric excitations and lock-in of flexible hydrofoils in two-phase flows," <u>Journal of Fluids and Structures</u>, Vol. 57, 2015, pp. 344-356.

Blasques J.P., Berggreen, C., and Andersen, P., "Hydroelastic analysis and optimization of a composite marine propeller," Marine Structures, Vol. 23, 2010, pp. 22-38.

Collins, J.M. and Matveev, K.I., 2019, "Exploratory tests of hydrofoil influence on air cavity under model boat hull," <u>Proceedings of the SNAME Maritime Convention</u>, 2019, Tacoma, WA, USA.

Ducoin, A., Deniset, F., Astolfi, J.A., and Sigrist, J.-F., "Numerical and experimental investigation of hydrodynamic characteristics of deformable hydrofoils," <u>Journal of Ship Research</u>, Vol. 53, 2009, pp. 214-226.

Ferziger, J.H. and Peric, M., <u>Computational Methods for Fluid Dynamics</u>, Springer, Berlin, 1999.

Giovannetti, L.M., Banks, J., Ledri, M., Turnock, S.R., and Boyd, S.W., "Toward the development of a hydrofoil tailored to passively reduce its lift response to fluid load," <u>Ocean Engineering</u>, Vol. 167, 2018, pp. 1-10.

Harwood, C.M., "The Hydrodynamic and Hydroelastic Responses of Rigid and Flexible Surface-Piercing Hydrofoils in Multi-Phase Flows," PhD Dissertation, University of Michigan, USA, 2016.

Hashin, Z., "Failure criteria for unidirectional fiber composites," <u>Journal of Applied Mechanics</u>, Vol. 47, 1980, pp. 329-334.

Hirt, C.W. and Nichols, B.D., "Volume of fluid (VOF) methods for the dynamics of free boundaries," <u>Journal of</u> Computational Physics, Vol. 39, 1981, pp. 201-225.

Keller, T., Henrichs, J., Hochkirch, K., and Hochbaum, A.C., "Numerical simulations of a surface piercing Aclass Catamaran hydrofoil and comparison against model tests," <u>Proceedings of the 22nd Chesapeake Sailing Yacht Symposium</u>, 2016, Annapolis, MD, USA.

Liao, Y., Garg, N., Martins, J.R.R.A., and Young, Y.L., "Viscous fluid-structure interaction response of composite hydrofoils," <u>Composite Structures</u>, Vol. 212, 2019, pp. 571-585.

Matveev, K.I., Wheeler, M.P., and Xing, T., "Numerical simulation of air ventilation and its suppression on inclined surface-piercing hydrofoils," <u>Ocean Engineering</u>, Vol. 175, 2019, pp. 251-261.

Rodi, W., "Experience with two-layer models combining the k-ε model with a one-equation model near the wall," <u>Proceedings of the 29<sup>th</sup> Aerospace Sciences Meeting</u>, 1991, Reno, NV, USA, AIAA paper 91-0216.

Shih, T.-H., Liou, W.W., Shabbir, A., Yang, Z., and Zhu, J., "A new k-ε eddy viscosity model for high Reynolds number turbulent flows," <u>Computers & Fluids</u>, Vol. 24, 1995, pp. 227-238.

Wheeler, M.P. and Matveev, K.I., "Numerical modeling surface-piercing flexible hydrofoils in waves," <a href="Proceedings of the SNAME Maritime Convention">Proceedings of the SNAME Maritime Convention</a>, 2019, Tacoma, WA, USA.

Wu, Q., Huang, B., Wang, G., and Cao, S., "The transient characteristics of cloud cavitating flow over a flexible hydrofoil," <u>International Journal of Multiphase Flow</u>, Vol. 99, 2018, pp. 162-173.

Xing, T. and Stern, F., "Factors of safety for Richardson extrapolation," <u>ASME Journal of Fluids Engineering</u>, Vol. 132, 2010, 061403.

- Ye, L., "Role of matrix resin in delamination and growth in composite laminates," <u>Composites Science and Technology</u>, Vol. 33, 1988, pp. 257-277.
- Young, Y.L., Garg, N., Brandner, P.A., Pearce, B.W., Butler, D., Clarke, D., and Phillips, A.W., "Load-dependent bend-twist coupling effects in the steady-state hydroelastic response of composite hydrofoils," Composite Structures, Vol. 189, 2019, pp. 398-418.
- Young, Y., Harwood, C., Montero, F., Ward, J., and Ceccio, S., "Ventilation of lifting bodies: review of the physics and discussion of scaling effects," <u>Applied Mechanics Reviews</u>, Vol. 69, 2017, 010801.
- Zarruk, G.A., Brandner, P.A., Pearce, B.W., and Phillips, A.W., "Experimental study of the steady fluid-structure interaction of flexible hydrofoils," <u>Journal of Fluids and Structures</u>, Vol. 51, 2014, pp. 326-343.

# **DISCUSSION**

Prof. Jeff D. Eldredge, Mechanical & Aerospace Engineering, University of California, Los Angeles.

The authors have performed a high-fidelity computational study of the effect of material properties – and particularly, the orientation of fibers in orthotropic materials – on a hydrofoil piercing the water surface. The work is extensive and very well done.

The results demonstrate that fiber orientation has a significant influence on many aspects of the hydrofoil's behavior and performance. Lift coefficient and lift-to-drag ratio both varied considerably as the fiber angle was changed between the extremes of -45 degrees and 45 degrees. It would be interesting to see the relationships between the structural deformations (twist, tip displacement) and the hydrodynamic performance (lift, lift-to-drag ratio) more directly.

Hydrofoils, as lifting surfaces, necessarily incur induced drag due to their tip vortices. This drag is likely affected by the structural deformation – but might there be benefits to particular orientations of fibers on mitigating this drag?

## **AUTHOR'S REPLY**

The authors thank Prof. Eldredge for interesting comments. The dependences of the lift coefficient and lift-drag ratio of orthotropic hydrofoils modeled in this paper on the twist and displacement at the tips of these hydrofoils in calm water are shown in Figures A1 and A2. One has to keep in mind that twisting and bending deformations are strongly coupled in the studied setups.

The lift coefficient is well correlated with the twist in almost linear fashion (Figure A1, top). This strong correlation is due to nearly linear dependence of the foil lift on the attack angle; and the effective attack angle is essentially proportional to the twist angle. The positive twist angles occurred at the negative fiber angles  $\theta < 0$  (i.e., when the fibers originating at the foil root were directed toward the foil trailing edge), as shown in Figure 11 in the paper. At large fiber angles (above 25° or below -25°), the lift coefficient values tend to be lower than those at smaller  $\theta$  at the same twist (Figure A1), which can be caused by additional effects due to pronounced tip displacements because of lower spanwise rigidity at high  $\theta$ . The lift coefficient dependence on the tip displacement (given in Figure A1, bottom) is masked to a large extent by the strong influence of the foil twist. Two main (and competing) effects of the tip displacement are the lift increase due to reduction of the foil dihedral and the lift decrease due to the foil approaching the free water surface. The latter effect is likely a dominant factor at large negative values of  $\theta$ , since the foil displacements become large, and with

lower effective submergence, the lift becomes smaller, which in turn leads to twist reduction.

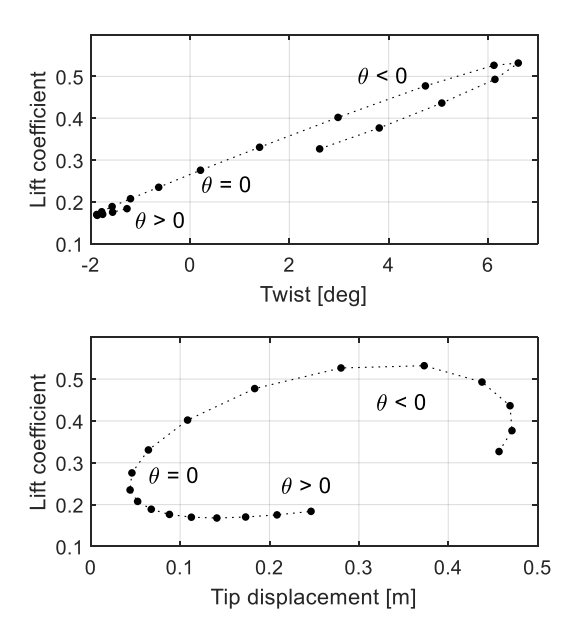
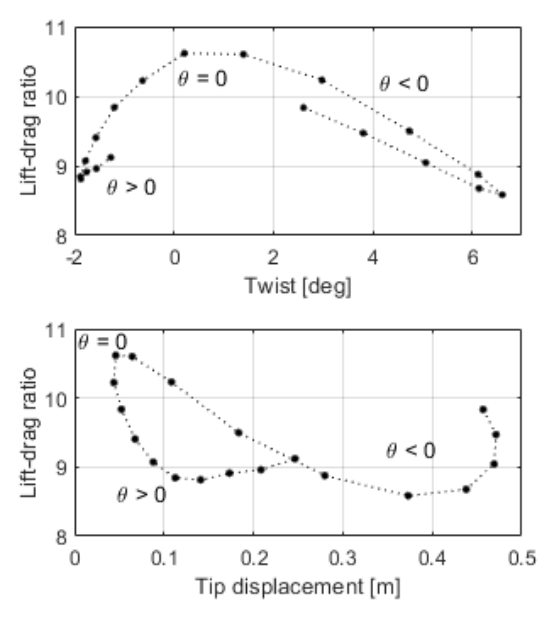


Figure A1: Variation of the foil lift coefficient with tip twist and displacement.



**Figure A2:** Variation of the foil lift-to-drag ratio with tip twist and displacement.

The lift-to-drag ratio shows well-defined maxima near zero twist and at minimal tip displacement (Figure A2). The decrease of LDR at both positive and

negative twist, as well as with increasing tip displacements, can be caused by departure of the effective attack angles from the optimal values and by the foil approaching the free water surface, which increases the wave drag. Similar to the lift coefficient, LDR is slightly smaller for large fiber angle magnitudes than for small  $\theta$  at the same twist (Figure A2, top), which can be associated with larger wave drag due to larger foil displacements. Some recovery of LDR at larger tip displacements (Figure A2, bottom) is likely caused by reduction of twist magnitudes, shifting the operational regime closer to optimal attack angles.

As possible future directions for coupled CFD-FEA simulations aimed at investigating fundamental hydroelastic effects, cases with decoupled twist and bending would provide more detailed information about these phenomena. Other variations of interests would include a range of attack angles, as well as horizontal hydrofoils at variable submergences.

The second point raised by Prof. Eldredge is on possibility of altering the tip vortices (associated with the induced drag) by using special fiber orientation. Instead of pre-twisted configurations, the unloading of the foil sections closer to the tip can be achieved by varying orientation of fibers along the foil span. For example, using fibers with positive  $\theta$  near the tip and with negative  $\theta$  closer to the root can achieve that goal. High-fidelity optimization of such sophisticated hydrofoil structures for specific operational regimes can be carried out using coupled CFD-FEA methods.

# **DISCUSSION**

Prof. Nikolai Kornev, Faculty of Mechanical Engineering and Ship Technology, University of Rostock, Rostock, Germany.

A very interesting paper of the authors is devoted to the influence of the flexibility of hydrofoils in steady and unsteady flow motions. The paper is well written and contains some findings clearly explained by the authors. It is shown that the effect of the fiber orientation on the lift coefficient and the pitching moment is very substantial. The lift can change by more than 100% due to generation of twisting caused by the hydrofoil flexibility. The results seem to be plausible because the authors used a well tried CFD and FE tools which they are additionally verified and validated for the hydrofoil applications. Although the resistance is by 20% underestimated (see Table 3) it is not critical for the present study, which focuses mainly on the lift properties.

The task is very complex because of the coupling between fluid dynamics and structural problems performed in time. Therefore, my question is whether it would be more pragmatic to couple the BEM

and FE, because I suppose the viscosity effects play a minor role for the problem under consideration. I realize that potential method could have problems for piercing foils because of the free surface breakdown. However, it could efficiently be damped by various numerical tricks.

I find very interesting the suggestion of the authors to achieve the self-regulation by the choice of the fiber orientation. As the authors noted, the composite hydrofoils that produce negative twist under hydrodynamic load would have smaller variations of the lift force in a range of speeds. They demonstrated this for the lift coefficient found at the same hydrofoil speed. Would be it more relevant to compare the lift force variations found for different wings generating the same mean lift? Indeed, the foils with a negative twist should move faster to generate the same mean lift and the lift variations at higher speed could be even larger.

### **AUTHOR'S REPLY**

The authors are thankful to Prof. Kornev for commenting on this paper. The first question is whether the coupled BEM and FEA method would be sufficient or even more attractive for practical design, given a high cost of computations involving viscous solvers. In our opinion, this simplified approach would indeed be convenient at the preliminary design stage, when parametric calculations in a broad range of conditions and system geometry are needed. Results obtained with a lower fidelity method could then be used for CFD-FEA simulations in a narrower range of system setups to obtain higher fidelity results. However, in some situations involving complex flow physics, e.g., with simultaneously happening flow separation (at high attack angles), breaking waves, cavitation and ventilation, the coupled BEM-FEA method is unlikely to produce reliable results. In these regimes, using CFD-FEA methods would be the only viable option. Moreover, trying more sophisticated but even more costly turbulent modeling approaches, such as LES, might be beneficial if sufficient computational resources are available.

The second question asks whether a foil with negative twist (N) will truly have lower lift variations when compared to a foil with positive twist (P), if these foils produce the same lift in a reference (initial) state. To analyze this problem, the standard lift equation can be used,

$$L = C_L \frac{\rho U^2}{2} S \,, \tag{A1}$$

where  $C_L$  is the lift coefficient,  $\rho$  is the water density, U is the speed, and S is the effective area of the foil. Assuming that both hydrofoils have the same attitude, produce the same lift, and their effective areas are the

same, the negative-twist foil will have to operate at higher speed,  $U_N > U_P$ , due to its lower lift coefficient,  $C_{LN} < C_{LP}$ .

To assess the lift variation with speed, one can derive the following expression from Equation (A1),

$$\frac{dL}{dU} = \frac{2L}{U\left(1 - \frac{L}{C_L} \frac{dC_L}{dL}\right)},\tag{A2}$$

where  $\frac{dC_L}{dL}$  is the lift coefficient sensitivity to the lift force variation caused by structural deformations. For the foil with negative twist,  $\left(\frac{dC_L}{dL}\right)_N < 0$ , whereas for the foil

with positive twist,  $\left(\frac{dc_L}{dL}\right)_P > 0$ , while the magnitudes of these sensitivities are assumed to be small, so that the absolute value of the second term inside parentheses in Equation (A2) is smaller than one. Due to the signs of these derivatives and the previous observation that  $U_N > U_P$ , it is evident from Equation (A2) that  $\left(\frac{dL}{dU}\right)_N < \left(\frac{dL}{dU}\right)_P$ , which implies that the speed-induced lift variation of the hydrofoil exhibiting negative twist will be smaller than that of the hydrofoil with positive twist.